

**DEDICATED TO MY FAMILY MEMBERS FOR THEIR
CONSISTENT SUPPORT, PASSION, UNDERSTANDING AND
ENCOURAGEMENT**



भारतीय
प्रौद्योगिकी
संस्थान
काशी हिन्दू विश्वविद्यालय



INDIAN
INSTITUTE OF
TECHNOLOGY
BANARAS HINDU UNIVERSITY

DEPARTMENT OF METALLURGICAL ENGINEERING

Indian Institute of Technology (BHU), Varanasi - 221005

Established by the Institutes of Technology (Amendment) Act, 2012 (No. 34 of 2012)

Phone : 0542-2307080-81, 2369346, Fax : 0542-2369478, email : head.met@iitbhu.ac.in

Date: 03/04/2024

CERTIFICATE

It is certified that the work contained in the thesis titled “**Structure-property correlations of the heat-treated and friction-stir processed AA7075T7352 alloy**” by “**Roopchand Tandon**” has been carried out under our joint supervision and that this work has not been submitted elsewhere for a degree.

It is further certified that the student has fulfilled all the requirements of Comprehensive, Candidacy and SOTA for the award of Ph.D. degree.

R.K.M. 2af
3/4/2024

Prof. R.K. Mandal

धातुक्रीय अभियांत्रिकी विभाग
(Supervisor)

Department of Metallurgical Engg

Department of Metallurgical Engineering

IIT (BHU), Varanasi - 221005

वाराणसी-221005/Varanasi-221005

Dr. R. Manna
3/4/2024

सह-अधीक्षक

(Co-supervisor)

Associate Professor

Department of Metallurgical Engineering

IIT (BHU), Varanasi - 221005

Indian Institute of Technology (Banaras Hindu University)

वाराणसी-221005/Varanasi-221005

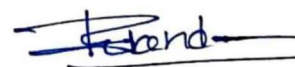
DECLARATION BY THE CANDIDATE

I, **Roopchand Tandon**, certify that the work carried out in the present thesis is my own work carried out under the supervision of **Prof. R.K. Mandal** and **Dr. R. Manna** for the period from July 2017 to March 2024 in the Department of Metallurgical Engineering IIT (BHU), Varanasi. The matter embodied in the thesis has not been submitted for the award of any degree or diploma.

I declare that I have faithfully acknowledged, given credit, and referred to the research workers wherever their work has been cited in the text and the body of the thesis. I further certify that I have not wilfully copied some other's work, paragraph, text, or data, as well as any observations, etc. Further, I haven't included any web data in the current thesis by citing the same as my work.

Date: 03/04/2024

Place: Varanasi



(Roopchand Tandon)

COPYRIGHT TRANSFER CERTIFICATE

Title of the Thesis: *“Structure-property correlations of the heat-treated and friction-stir processed AA7075T7352 alloy”*

Candidate’s Name: Roopchand Tandon

COPYRIGHT TRANSFER

The undersigned hereby assigns to the Indian Institute of Technology (BHU), Varanasi, all rights under copyright that may exist in and for the above thesis submitted for the award of the **Ph.D. Degree**.

Date: 03/04/2024

Place: Varanasi



(Roopchand Tandon)

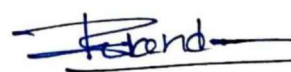
Note: However, the author may reproduce or authorize others to reproduce materials extracted verbatim from the thesis or derivative of the thesis for the author's personal use, provided that the source and the institute’s copyright notice are indicated

Acknowledgements

Firstly, I would like to express my sincere gratitude to my supervisor, **Prof. R.K. Mandal**, and co-supervisor, **Dr. R. Manna**, for their consistent support, motivation, and valuable discussions during the study. His guidance helped me throughout the research and writing of this thesis.

I am thankful to Prof. Suneel Mohan, Head of the Department of Metallurgical Engineering, and former Head of the Department, **Prof. N.K. Mukhopadhyay**, for their valuable input and permission to use the department facilities. Besides my supervisors, I would like to especially thank the other members of RPEC: **Prof. Mohd Zaheer Khan Yusufzai**, Department of Mechanical Engineering, and **Dr. A. K. Mondal**, Department of Metallurgical Engineering, for their insightful comments and encouragement, which helped me a lot to widen my research from various perspectives. Very special gratitude goes to **Dr. K.K. Mehta** for providing materials and necessary discussion. **Dr. Sudipta Patra** is acknowledged for their help attributed to the EBSD and Bulk texture analyses. **Dr. Joysurya Basu** is acknowledged for the TEM and SEM training, and Prof. Shanthi Srinivas for their help related to mechanical testing and characterization. I want to thank all other faculty members of the Department of Metallurgical Engineering IIT (BHU) for their cooperation and inspiration. I am thankful to all my batchmates and friends: Shravan Kumar, Sandeep Gupta, Jaydeep Vishwakarma, Amit Kumar Singh, Nitesh Sinha, Shanker Kumar, Ankur Sharma from IIT Bombay, Priyatosh, Ketan, Sakshi, Urwashi Gupta, Bhumika, Vikrant and Deelip . Senior colleagues Dr Manish Kumar Singh, Ankit Singh, Avanish Singh Pal, Aman Kumar Lal Das, Mr. Yagnesh Shadangi, and CV Rao are acknowledged for their help in different ways. I would like to thank all my Labmates, Soham Mukherjee, Satyam Chowdhay, Saptarshi Mukherjee, Priyatosh Pradhan, Rajat Gupta, and Sarika Shah for their cheerful and lovely company. I also

would like to thank Mr. Mithilesh Kumar Mahto, a research scholar in mechanical engineering, for their valuable help. My junior M. Tech and Ph.D. students during the overall tenure of work are also acknowledged. I would like to extend my sincere thanks to the entire Lab and non-teaching staff, especially Mr. Lalit Kumar Singh, Mr. Anjani Kumar Singh, Shri Ram Ashre, Mr. Ashok Kumar, Shri Minj ji, Mr. Arun Prakash, Mr. Ramesh Kumar, Mr. Jay Prakash Patel, Mr. Sushil Kumar, and Mr. Balwant Singh for their kind help during work. Shri Kamlesh Mishra is especially acknowledged for their help in mechanical testing and characterization. I am grateful to Prof. Rajiv Prakash and Prof. K.K. Singh (Prof. in charge) of Central Instrument Facility IIT (BHU) for providing the characterization facilities and his technical teams, especially Mr. Girish Sahu Ji. Dr. Sumanta Bagui, Senior Scientist DMRL, is acknowledged for the low cycle fatigue test. **Prof. I. Samajdar**, IIT Bombay (OIM-Texture National Facility), is acknowledged for extending the micro-texture (EBSD) characterization facility. Finally, last but by no means least, I would like to express my deepest gratitude to my family, especially my father, **Shri Munnalal Tandon**, and my mother, **Smt. Bishmat Tandon**, for his support, care, sacrifice, and encouragement in pursuing my interest. I would also like to thank my younger brothers, **Bhagwati Prasad Tandon, Rupesh Kumar Tandon, and Rahul Tandon**, for their care and support in all my decisions during the PhD Journey. I also would like to thank all my friends and the persons whose names have not been mentioned on this piece of paper for extending their cooperation directly or indirectly. Above all, I bow my head before **'The God Almighty'**, who blessed me with good health and confidence to undertake and complete the work successfully.



Roopchand Tandon

Contents

	Page No.
Acknowledgements	[v-vi]
Contents.....	[vii-xii]
List of Figures	[xiii-xx]
List of Tables	[xiii-xxi]
List of Symbols.....	[xxiv-xxv]
Abbreviations	[xxvi-xxvii]
Preface	[xxviii-xxxvii]
Chapter 01	
Introduction and knowledge gaps	1
1.1 Introduction.....	2-3
1.2 Types of the Al-alloys.....	3-8
1.3 Characteristics of the Al-alloy.....	9
1.4 Development of the Al-Cu (2xxx) alloy.....	10-11
1.5 Development of the Al-Li alloy.....	12-14
1.6 Development of the Al-Mg-Si (6xxx) alloy.....	14-15
1.7 Development of the Al-Zn-Mg-Cu (7xxx) alloy.....	15-17
1.8 Applications of the 7xxx Al-alloy in aviation industries.....	18-19
1.9 Specific properties of 7xxx series Al-alloy.....	19-21
1.10 Phase diagrams of heat-treatable Al-alloys.....	21-23
1.11 Phase diagrams of the non-heat-treatable Al-alloys.....	24-25
1.12 Precipitation in age hardenable Al-alloys.....	25
1.13 Precipitation in 2xxx series Al-alloys.....	26-27
1.14 Precipitation in 7xxx series Al-alloys.....	27-28
1.15 Factors influencing the morphology, size, and shape of precipitates.....	28-29

1.16	Effects of alloying addition on microstructures and mechanical properties of the aged Al-alloy.....	30-32
1.16.1	Additions of Cu+Mg.....	30-31
1.16.2	Additions of the Zr.....	31
1.16.3	Additions of the Mg+Zn.....	31-32
1.16.4	Addition of the Ti.....	32
1.16.5	Addition of the Cr.....	32
1.17	Microstructural features of the aged 7xxx series Al-alloy.....	32-34
1.18	Mechanical properties of aged 7xxx series Al-alloys.....	34-35
1.19	Microstructures and stress corrosion cracking.....	36-37
1.20	Dislocation structures in cubic-fcc-based metals and alloy.....	37
1.21	Effect of friction-stir processing on microstructure evolution.....	37-40
1.22	Textures in cubic fcc-based metals and alloys.....	40-44
1.23	Micro textures in 7075 Al-alloys.....	44-45
1.24	Structural phase transformations in age-hardenable Al-alloys.....	45-46
1.25	Types of interfaces in age hardenable Al-alloys.....	46-48
1.26	Strengthening mechanisms in age hardenable Al-alloy.....	48-54
1.26.1	Grain size strengthening.....	48
1.26.2	Solid solution strengthening.....	49
1.26.3	Dislocation strengthening.....	50
1.26.4	Precipitation strengthening.....	50-53
1.26.5	Strengthening by dispersoids and other factors.....	54
1.26.6	AA7075T7352 design objectives.....	55
1.27	Methods of improving the performances of 7xxx series of Al-alloys....	55-61
1.28	Knowledge gaps	56-58
1.28.1	Knowledge gaps attributed to the precipitation behavior.....	55-58
1.28.2	Knowledge gaps about dislocation structures.....	59
1.28.3	Knowledge gaps related to thermo-mechanical processing	60
1.28.4	Knowledge gaps attributed to friction-stir processing.....	60-61
1.29	Objectives.....	62

Chapter 02

Materials and experimental methods63
2.1 Introduction.....	...64-65
2.2 Materials	65-66
2.3 Heat treatments.....	66-67
2.4 Interrupted test.....	67-68
2.5 Thermo-mechanical processing.....	68-69
2.6 Friction-stir processing	69-74
2.7 Structural and microstructural characterization.....	74-75
2.8 Optical microscopy.....	75-77
2.9 X-ray diffraction.....	77-79
2.10 Bragg's Brentano geometry.....	80-81
2.11 Determination of lattice micro-strain (ϵ), crystallite size (D in \AA), and dislocation density.....	81-83
2.12 Residual stress and bulk texture measurements	83-84
2.13 Bulk texture	84
2.14 Bulk texture measurement.....	85
2.14.1 Pole figure (PF)	85
2.14.2 Inverse pole figure (IPF).....	85
2.14.3 Orientation distribution function (ODF).....	86-87
2.15 Scanning electron microscope.....	88-90
2.15.1 Emission of various electrons and their significance.....	90
2.15.2 Micro-texture characterization using EBSD.....	90
2.15.3 Measurements of the microtexture.....	92
2.15.4 Electron back-scattered diffraction (EBSD).....	92
2.15.5 Components of the EBSD.....	94
2.15.6 Formation of the Kikuchi Pattern	95-96
2.15.7 Bright and dark Kikuchi lines.....	96-97
2.16 Structural characterization.....	97
2.16.1 TEM sample preparation technique.....	98
2.16.2 Transmission electron microscope.....	99-100
2.16.3 TEM investigation of the metastable precipitates.....	101-103
2.16.4 Diffraction contrast imaging.....	103-104

2.16.5 Bright and dark-field TEM imaging	105-106
2.17 Weak-beam dark-field (WBDF)TEM imaging.....	106-107
2.17.1 Working principles	107-109
2.17.2 Methods of obtaining the weak-beam condition.....	109-110
2.18 Phase contrast imaging.....	110-112
2.19 HAADF STEM or Z-contrast imaging.....	112-113
2.20 X-ray energy dispersive spectroscopy (XEDS).....	114-115
2.21 Mechanical characterization.....	115-120
2.21.1 Conventional hardness test	115
2.21.2 Vickers microhardness test.....	116
2.21.3 Instrumented microhardness test.....	116-117
2.21.4 Tensile test	117-118
2.21.5 Stress corrosion cracking	118-119
2.22 Software details	120

Chapter 03

Effect of microstructure and texture on mechanical behaviors of the heat-treated AA7075T7352.....

3.1 Introduction	122-127
3.2 Results	127
3.2.1 Part I Electron microscopy of precipitates in AA7075T7352.....	127-147
3.2.2 Part II Effect of tensile straining on the precipitation and dislocation behaviors of the AA7075T7352	147-163
3.2.3 Part III Comparative microstructures, textures, flow behavior and mechanical properties of the aged 7075 Al-alloy.....	163-190
3.4 Discussion	190
3.4.1 Part I Electron microscopy of precipitates in AA7075T7352.....	190-195
3.4.2 Part II Effect of tensile straining on precipitation and dislocation behaviors of the AA7075T7352.....	195-203
3.4.3 Part III Comparative microstructures, textures, flow behavior, and mechanical properties of aged 7075 Al-alloy	203-214
3.5 Conclusions	215

3.5.1 Part I Electron microscopy of precipitates in AA7075T7352.....	215
3.5.2 Part II Effect of tensile straining on precipitation and dislocation behaviors of the AA7075T7352.....	215-216
3.5.3 Part III Comparative microstructures evolution, texture characteristics, mechanical properties and flow behaviors of aged 7075 Al-alloy.	216-218

Chapter 04

Microstructure, texture, and mechanical behaviors of the cold-rolled 7075 al-alloy followed by the peak-ageing.....219

4.1 Introduction	220-222
4.2 Results.....	222
4.2.1 XRD analysis.....	222-227
4.2.2 Bulk texture characterization.....	227-231
4.2.3 Microtexture characterization.....	232-235
4.2.4 TEM analysis	236-238
4.2.5 Nature of precipitates and solutes.....	238-239
4.2.6 Mechanical properties	239-242
4.2.7 Flow behaviors	242-250
4.2.9 Fractography analysis	250-252
4.3 Discussion	252-259
4.4 Conclusions.....	-260

Chapter 05

Evolution of the microstructures and textures of friction-stir processed AA7075T7352 and their effects on mechanical properties.....261

5.1 Introduction.....	262-265
5.2 Results.....	266
5.2.1 Optical micrograph.....	266
5.2.2 XRD and DTA analysis	266-271
5.2.3 Microtexture	271-284
5.2.4 TEM analysis	285
5.2.4.1 TEM analysis after 1 pass FSP.....	285-292
5.2.4.2 TEM analysis after multi-pass FSP.....	292-299

5.2.5 STEM EDS elemental mapping	299-303
5.2.6 Mechanical properties.....	303
5.2.6.1 Hardness and residual stress.....	303-306
5.2.6.2 Tensile properties	306-315
5.2.7 Fractography.....	316-317
5.3 Discussion	317-329
5.4 Conclusions.....	330

Chapter 06

Summary and suggestions for future work.....331-340

6.1 Introduction.....	332
6.2 Summary	332-340
6.2.1 Summary of precipitation behavior.....	332-334
6.2.2 Summary of the dislocation characteristics.....	335
6.2.3 Summary of the textures.....	335-36
6.2.4 Summary of the residual stress and hardness.....	337-38
6.2.5 Summary of the mechanical properties and flow behaviors.....	338-339
6.2.6 Summary of the stress corrosion cracking.....	339
6.3 Suggestions for the future work	340

References

341-364

List of the publications

367

List of the conferences/workshops.....

368-6

List of Figures

Figures No.	Captions	Page No
Fig. 1.1	Heat-treatable and non-heat-treatable Al-alloys	4
Fig. 1.2.	Requirements of age-hardening: (a) decreasing solid solubility of Cu with temperature, (b) formation of semi-coherent (θ'), and incoherent (θ) phases	9
Fig. 1.3	The plots show increased modulus of Al-Li alloys along with year of introduction	14
Fig.1.4	Wings upper skin alloys and heat treatments used for manufacturing of passenger aircraft between 1919 and 1994	17
Fig. 1.5	Properties and major applications of 7xxx series Al-alloys in structural engineering applications	20
Fig. 1.6	Phase diagrams of heat-treatable Al-alloys: (a) Al-Cu (2xxx series), (b) Al-Si-Mg (6xxx series), and (c) Al-Zn (7xxx) series	22
Fig. 1.7	Phase diagram of Al-Mn (3xxx series) of non-heat-treatable Al-alloy	24
Fig. 1.8	Precipitation in age hardenable Al-Cu alloys (Duralumin Al 4.5% Cu alloy)	27
Fig. 1.9	Shape factors as a function of axial ratio for the ellipsoidal precipitates	29
Fig. 1.10	Formation of PFZs, and intermetallic $Al_3(Zr, Ti, Sc)$ after alloying additions	31
Fig. 1.11	Bright-field TEM micrograph of (a, b) peak-aged (c) T76 (d) T73 and (e, f) TEM microstructures of 7075 Al-alloy after RRA	34
Fig. 1.12	Tensile properties of heat-treated 7075Al-alloy in T4, T6, T73, and highly over-aged conditions	35
Fig. 1.13	Schematic details of friction stir processing, consisting of the tool, workpiece, and the processed region	39
Fig. 1.14	Microstructural variation throughout the processed zones: (a) macrostructures, (b) nugget zone, (c) thermo-mechanically affected zone (TMAZ), heat affected zones (HAZ), and the base-metals (BM)	40
Fig. 1.15	Plots of important fiber textures in FCC-based metals, and alloys	43
Fig. 1.16	Compositional variation during nucleation and growth-assisted structural phase transformations	46
Fig. 1.17	Heterophase and homophase structures in metastable precipitates of 7075Al-alloy	48
Fig. 1.18	Coherent precipitates vs. dislocation interaction with less size (50Å)	52
Fig. 1.19	Dislocation precipitate interaction if precipitates are more than 100Å to 500Å in size	53

Fig. 1.20	Contributions of the hardening factors in the Al-Li alloys	54
Fig. 1.21	Techniques used for improving the performances of the 7075 Al-alloy	55
Fig. 1.22	Precipitates in 7xxx series of Al alloy: (a) solute-rich clusters, (b) metastable precipitates (GP zone, η' and η), (c) vacancy-rich clusters, (d) plate-like morphology of GP zone	57
Fig. 1.23	Metastable precipitation in 7xxx series Al-alloy: (a) spherical precipitates, (b) rod-like (η') phase, (c,d) plate-type η precipitates	58
Fig. 1.24	Diffraction spots of 7075 Al-alloy showing GP I, and Al_3Zr dispersoids	58
Fig. 1.25	Dislocation structures in FCC-based cubic metals and alloys: (a,b) dislocation loops, (c) Taylor lattices, (d,e) dislocation array, (f,g) cellular structures	59
Fig. 2.1	Schematic of heat treatment: (a) under-aging T4, (b) peak-aging T6, (c) over-aging T73, and (d) T7352 temper.	67
Fig. 2.2	The schematic details of heat treatment and thermo-mechanical processing: (a) SQ, (b) T6, (c) TMP-1, (d) TMP-2, and (e) TMP-3.	69
Fig. 2.3	Schematic details of working principles of FSP	71
Fig. 2.4	Schematic of friction stir processing: experimental set-up and specimen before processing (a), friction stir processed specimen (b), a tool used during the processing (c), and surface appearance before and after friction stir processing (d,e).	72
Fig. 2.5	Schematic of the different combinations of friction stir processing (FSP).	73
Fig. 2.6	Schematic diagram of the friction-stir processed plate: the location of specimens for various characterization is displayed, LD, TD, and ND represent the longitudinal, transverse, and normal directions, respectively, BM, AS, and RS, are base-metal, advancing, and retreating sides. NZ, and HAZ, depict serially the nugget zone and heat-affected zones.	74
Fig. 2.7	Schematic of the optical microscope: showing the visible light source, objective, and condenser lenses	77
Fig. 2.8	Schematic of the working principles of XRD in θ -2 θ geometry	78
Fig. 2.9	Schematic of working principles of XRD in Bragg's Brentano geometry	81
Fig. 2.10	Difference between the stereogram and the pole figure: (a) stereogram and (b) pole figure	85
Fig. 2.11	Wire-drawn axes and respective IPF, orientation contour will form near 110 in IPF	86
Fig. 2.12	Schematic of the specimen reference frame and crystal reference frame	88

Fig. 2.13	Schematic of the SEM: a) Front half section, b) electron beam trajectory	89
Fig. 2.14	Emission of various electrons from the sample surface, while specimen-electron interaction	90
Fig. 2.15	Schematic of the EBSD geometry showing the pole piece of SEM, the electron beam, the tilted specimen, and the phosphor screen	94
Fig. 2.16	Formation of the backscattered Kikuchi patterns by EBSD in SEM	96
Fig. 2.17	Twin jet electro-polishing setup and their working principle	98
Fig. 2.18	Path of the electron beam in TEM when high voltage is applied to the electron source	101
Fig. 2.19	Schematic of the imaging and diffraction mode of operation in TEM: (a) diffraction mode, and (b) imaging mode.	104
Fig. 2.20	Schematic of imaging technique:(a) bright-field (b) dark-field TEM imaging	106
Fig. 2.21	Schematic of DPs in WB condition after suitable tilting, $g(220)$ reflection is a weak beam, and $3g(220)$ shows a strong beam.	108
Fig. 2.22	Relationship between the orientation of the Ewald sphere, and the position of the Kikuchi lines: $0(g)$ (A and B) and $g(3g)$ (C and D) in WB condition.	110
Fig. 2.23	Schematic of HRTEM mode of operation (phase contrast imaging).	112
Fig. 2.24	Schematic representation of HAADF-STEM or the Z-contrast imaging	113
Fig. 2.25	Schematic of STEM EDS detector, and a few other detectors used for the analytical characterization	115
Fig. 2.26	Schematic details of tensile specimens (all dimensions are in mm)	118
Fig. 3.1	X-ray diffraction pattern of the AA7075T7352 Al-alloy.	128
Fig. 3.2	Lattice positions of cubic α -Al (a), hcp structures $MgZn_2$ (b), Al_2CuMg (c), and Al_2Cu phase (d).	130
Fig. 3.3	Precipitation behavior: (a)bright-field TEM micrograph, (b)corresponding SAEDP along the $[111]$ of Al zone – axis, (c) dark-field TEM micrograph corresponding to diffraction spot DF1, (d) dark-field TEM micrograph from diffraction spot DF-2, (e)bright-field TEM images from another region, (f) corresponding SAEDPs along the $[111]_{Al}$ zone-axis, (g) dark-field TEM images from DF-3, (h) dark –field TEM images from DF-4.	132-133
Fig. 3.4	(a) HRTEM image of plate type η precipitate, (b)FFT from the selected region of precipitate, (c) respective IFFT TEM image.	135
Fig. 3.5	HAADF STEM-EDS of η' and η precipitates: (a) HAADF image of η' precipitates joining in the interface, (b, c) analyzed	136-137

	chemistry in STEM mode, showing Zn map in (b), and Mg map in (c), (d) HAADF image of η phase, (e,f,g) analyzed chemistry in the STEM mode, display Zn rich map in (e), Mg-rich map in (f), and Zr rich map in (g).	
Fig. 3.6	Precipitation behavior: (a) bright-field TEM images,(b)corresponding SAEDPs~ along $[112]_{Al}$ zone-axis, (c)dark-field TEM image from DF-5, (d)dark-field TEM image from DF-6, (e) bright-field TEM image from another area, (f) respective SAEDPs~ along $[112]_{Al}$, (g) dark-field TEM image from spot DF-7.	139-140
Fig. 3.7	Precipitation behavior: (a)bright-field TEM micrograph, (b)corresponding SAEDP along the $[110]_{Al}$ zone axis, (c)dark-field TEM micrograph from diffraction spot DF-8.	141
Fig. 3.8	STEM EDS area mapping of precipitates in AA7075T7352, the presence of the Zn, Mg, and Cu-rich precipitates are observed	142
Fig. 3.9	HAADF STEM-EDS elemental mapping of precipitates in AA7075T7352, from the region consisting of spherical, rod, plate, and lath type precipitates: (a) HAADF Image, (b) Al map, (c) Zn map, (d) Mg map, (e) Cu map, (f) Zr map and (g) energy count map of the region	143
Fig. 3.10	Spectrum of precipitates in AA7075T7352(a), chemistry of spectrum 1(b), chemistry of spectrum 2	144-145
Fig. 3.11	HRTEM images (a), respective fast Fourier transform (FFT) diffractogram (b), inverse fast Fourier transform (IFFT) (c), FFT from region 2(d), IFFT from region 2.	147
Fig. 3.12	X-ray diffraction patterns of the as received as well as partially tensile strained specimens: (a) as received AA7075T7352 Al-alloy, (b) Partial tensile true straining corresponding to 0.02, (c) Tensile true straining corresponding to 0.06, and (d) Tensile true strain corresponding to 0.1,(e-h) enlarged XRD patterns of the partially deformed specimens between 39° to 44° .	148-149
Fig. 3.13	Precipitation behavior: (a, c, e, g,) bright-field TEM micrograph of the as-received as well as tensile strained specimens D1, D2, and D3 respectively, (b, d, f,h) their corresponding selected area electron diffraction patterns respectively.	152-153
Fig. 3.14	Dislocation behavior of D1 (true strain~ 0.02): (a) diffracted, 111 g-vector when after tilting, (b,c) bright-field TEM micrographs from the same region, b showing dislocation loops, c displaying forest dislocation and high-density dislocation tangles, (d,e) weak-beam dark-field (WBDF) TEM micrograph from 2g, DF-1 and 3g, DF-2(encircled in yellow) respectively, dislocation loops and tangles were observed respectively.	155

Fig. 3.15	Dislocation behavior of D2 (true strain 0.06): (a) diffracted, 200 g-vector after suitable tilting for weak beam condition. (b,c) bright-field TEM micrographs from the same region, showing Taylor Lattice structures with low and high dislocation density respectively, (d,e)WBDF TEM micrographs from 2g, DF-3, and 3g, DF-4 (encircled in yellow) showing broad and narrow Taylor lattices respectively.	157
Fig. 3.16	Dislocation behavior of D3 (true strain ~0.1): (a) diffracted, 220 g-vector after suitable tilting. (b,c) bright-field TEM micrographs from the same region, b showing low-density dislocation cell structure, c showing high-density dislocation cell structures (d,e) Weak beam dark field TEM Micrograph from the -g, DF-5 and -2g, DF-6 (encircled in yellow) diffracted beam, Low and high-density dislocation cell structures were seen respectively (color figure online).	158
Fig. 3.17	Schematic of diffracted g-vector and Burger vectors of the dislocation loops projected along the [000] zone-axis.	159
Fig. 3.18	Tensile properties of the elongated specimen D_1 till the fracture: (a) engineering stress-engineering strain plot, (b) true stress-true strain plot (c) logarithmic plot of the true stress-true strain (d) Ludwigson curve fitting of the logarithmic plot (true stress-true plastic strain), (e) hardening rate- true plastic strain curve behavior	161
Fig. 3.19	Hardening rate versus true plastic strain plot in the 3 rd - stage showing the linear relationship with slight fluctuation	162
Fig. 3.20	Fracture morphologies of the tensile specimen D_1 . One sees the facet/cleavage morphology in Fig. 3.20a. Whereas, dimples and micro voids, as well as particle cracks, were noted in Fig. 3.20b. On the other hand, dimple ruptures were seen in Fig. 3.20c.	163
Fig. 3.21	XRD pattern of heat-treated 7075 Al-alloy: (a) under-aged (T4) state, (b) peak-aged (T6) condition, (c) over-aged (T73) state, and (d) T7352 temper.	165
Fig. 3.22	Orientation distribution function (ODF) $\Phi_2 = 0^\circ, 45^\circ, 65^\circ$ and 90° sections (Bunge notation) of the T4 (a), T6 (b), T73 (c), and T7352 temper (d).	167
Fig. 3.23	Grain size variation of (a, b, c, d) T4, T6, T73, and T7352 tempers, (e, f) color-coded grain map/ inverse pole figure of T73 and T7352.	168
Fig. 3.24	Misorientation angle of: (a) under-aged(T4) alloy, (b) peak-aged (T6) alloy, (c) over-aged(T73) alloy, and (d) T7352 tempered alloy	169
Fig. 3.25	TEM microstructure: (a, c, e, g) bright-field TEM micrograph at T4, T6, T73, and T7352 tempers, (b, d, f, h) respective selected area electron diffraction patterns (SAEDPs~).	171-172

Fig.3.25.1	Nature of the grain boundary precipitates: (a) T4, (b) T6, (c) T73, and (d) T7352 tempers.	174
Fig. 3.26	TEM microstructure: (a, b) bright-field TEM micrograph, (c) diffracted weak beam (2-beam), and, (d) weak beam dark-field (WBDF) TEM images from “2g” show dense dislocation walls (DDWs~) and slip-band.	176
Fig. 3.27	Variation of hardness (Hv), and residual stress (MPa) of heat-treated 7075 Al alloy	177
Fig. 3.28	Tensile properties: engineering stress-engineering strain behaviors heat-treated alloy.	178
Fig. 3.29	Logarithmic true stress vs. logarithmic true plastic strain curve (Log 10 scale): (a) T4, under-aged, (b) T6, Peak-aged, (c) T73, over-aged, and (d) T7352 temper, deformed after solution treatment and two steps of the ageing treatment.	183
Fig. 3.30	Variation of logarithmic strain hardening rate $\ln(d\sigma/d\varepsilon, \theta)$ concerning logarithmic corrected true plastic strain $\ln(\varepsilon_0+\varepsilon_p)$: (a) T4, (b) T6, and (c) T73, (d) Strain hardening rate, $d\sigma/d\varepsilon_p (\theta)$ concerning true plastic strain (ε_p).	184-187
Fig. 3.31	Fracture behavior, SEM secondary electron images: (a) T4, (b) T6, (c) T73, and (d) T7352 tempers.	189
Fig. 3.32	Load vs. elongation behavior of AA7075, at T7352 and T73 tempers in the air, and 3.5% NaCl solution.	190
Fig. 4.1	XRD Peaks of heat treated (SQ, and T6) alloy: (a) 2θ range of 15° to 85° , (a ₁) 2θ range of 39° to 43° , and (a ₂) 2θ range of 46.5° to 49.5° .	223
Fig. 4.1	XRD peaks after thermo-mechanical processing: (b) XRD peaks in a 2θ range of 15° to 85° (full range), (b ₁) magnified view of 111 reflections showing left shift from TMP-1 to TMP-3, (b ₂) magnified view in 2θ range of 41.2° to 43° , (b ₃) magnified view in 2θ range of 46.3° to 48.2° . The top shows TMP-1, middle TMP-2, and bottom depicts TMP-3.	225-26
Fig. 4.2	Pole figures, 111, 200, and 220 of (a) solution quenched (SQ), (b) (T6), (c) TMP-1, (d) TMP-2, and (e) TMP-3.	225
Fig. 4.3	Bulk texture, orientation distribution function, (ODF) $\Phi_2 = 0^\circ, 45^\circ$ and 65° sections of (a) SQ alloy, (b) T6 alloy (c) TMP-1, (d) TMP-2, and (e) TMP-3.	227
Fig. 4.4	Microtexture, ODF $\Phi_2 = 0^\circ, 45^\circ$ and 65° sections of T6 (a), TMP-1 (b), TMP-2 (c), and TMP-3 (d).	233
Fig. 4.4.1	Super-imposed grain boundary maps: (a) peak-aged (T6), (b) TMP-1, (c) TMP-2, and (d) TMP-3.	234
Fig. 4.4.2	Co-incident site lattice (CSL) boundary fractions of (a) peak-aged (T6) alloy, (b) TMP-1, (c) TMP-2, and (d) TMP-3.	235

Fig. 4.5	Bright-field TEM micrograph of SQ and T6 (a,b), and respective selected area electron diffraction patterns (c,d), bright-field TEM micrograph of TMP-1, TMP-2 and TMP-3 (e, g, i), corresponding SAEDPs~ (f, h, j).	236-37
Fig. 4.6	Hardness and residual stress for the T4, T6, TMP-1, TMP-2, and TMP-3 tempered 7075 Al alloy.	240
Fig. 4.7	Engineering stress-engineering strain behavior of heat-treated (SQ and T6) alloys as well as TMP-1, TMP-2, and TMP-3.	241
Fig. 4.8	Fitted flow curves using mathematical models: (a) SQ, (b) T6, (c) TMP-1,(d) TMP-2, and (e) TMP-3.	243
Fig. 4.9	Logarithmic hardening rate, $\ln(d\sigma/d\varepsilon_p)$ versus true plastic strain $\ln(\varepsilon_0+\varepsilon_p)$ plot of the Swift fitted curves (a,b,c), and Ludwigson fitted curves (d,e).	246-49
Fig. 4.10	SEM micrograph fracture surface of: (a,b) SQ alloy, and (c,d) peak-aged (T6) alloy.	251
Fig. 4.11	Fracture surface after TMP: (a, b) TMP-1, (c, d) TMP-2, and (e,f) TMP-3.	252
Fig. 5.1	Optical microstructure after FSP : (a) base-metal (R.S.), (b) Interface, consisting of the N.Z., HAZ, and base-metal, and (c) nugget-zone.	266
Fig. 5.2	XRD peaks of (a) as-received, (b) 1pass FSP, (c) 2pass FSP, and (d) 3passes of FSP, (e) XRD peaks (111) of α -Al, after multi-pass FSP, in 2θ range of 38° to 39.5° , peaks in 1pass & 2pass FSP shifted toward the right, but after 3passes FSP, the peak was shifted to the left, (f) DTA thermogram up to 773K from three different zones of the NZ, HAZ, and BM after FSP.	268-271
Fig. 5.3	Orientation distribution function (ODF), $\Phi_2 = 0^\circ, 45^\circ, 65^\circ$ sections (a) base-metal, (b) 1pass FSP, (c) 2pass FSP, and (d) 3passes FSP.	272-278
Fig. 5.4	Grain size, and misorientation angle plot of multi-pass FSP: (a,c,e) grain size versus area fraction maps, and (b,d,f) misorientation angle vs. number fraction maps.	280
Fig. 5.5	Micro-texture characteristics/color-coded grain maps: (a,b,c,d) inverse pole figure map, and (e,f,g,h) KAM map of AR alloy and after 1 pass FSP, 2pass FSP and 3 pass FSP.	281
Fig. 5.6	111, 200, and 220 pole figures of (a) base metals, (b) 1pass FSP, (c) 2passes of FSP, and (d) 3passes FSP. A1 displays the rolling direction, and A2 shows the transverse direction.	282
Fig. 5.7	Kernel average misorientation (KAM) maps of (a) AR alloy (BM), (b) 1 pass FSP, (c) 2 pass FSP, and (d) 3 pass FSP.	283
Fig. 5.8	CSL boundary fractions of (a) AR alloy, (b) 1pass FSP, (c) 2pass FSP, and (d) 3pass FSP.	284

Fig. 5.9	TEM micrograph of AR alloy: bright field TEM micrograph and respective SAEDPs along 001 of α -Al (a,b), bright field TEM micrograph, and corresponding SAEDPs along 110 of α -Al	286
Fig. 5.10	Dislocation behavior: (e) bright-field TEM micrograph, (f) corresponding DPs~, (g, h) WBDF-TEM micrograph from g and 2g, respectively.	287
Fig. 5.11	bright-field TEM micrograph of the top of nugget-zone (a), respective SAEDPs (b), dark field TEM micrograph from g (c), and DF TEM micrograph from 2g (d).	289
Fig. 5.12	Dislocation behavior from the middle portion of the NZ: (a) bright-field TEM micrograph, (b) respective SAEDPs in 3-beam condition, (c) WBDF-TEM micrograph from "2g", and (d) WBDF-TEM micrograph from "3g".	290
Fig. 5.13	Precipitates morphology and dislocation behavior at the interface after FSP: (a, c) bright-field TEM micrographs, and (b,d) corresponding SAEDPs~.	292
Fig. 5.14	TEM micrograph of as-received specimen: (a) bright-field TEM images, (b) corresponding SAEDPs~, (c) dark field TEM image.	293
Fig.5.14.1	(a, c) bright-field TEM micrographs of the top portion of the NZ and (b, d) respective DPs.	294
Fig. 5.15	TEM micrograph, after 2pass FSP, along 111 of α -Al: (a) bright-field TEM image, (b) corresponding SAEDPs, (c) dark field TEM micrograph.	295
Fig. 5.16	TEM micrograph, after 3pass FSP, along 111 zone-axis of α -Al: (a) bright-field TEM image, (b) corresponding SAEDPs, (c) dark field TEM image.	296
Fig. 5.17	bright and dark field STEM micrograph of (a, b) AR alloy, (c,d) 1pass FSP, (e,f) 2pass FSP, (g,h) 3pass FSP.	298-299
Fig. 5.18	Spectrum area mapping of precipitates in AR state: (a) bright-field STEM micrograph, (b) spectrum of elements from the selected area of precipitates	300
Fig. 5.19	STEM-EDS elemental mapping of precipitates in AR state: (a) bright-field STEM micrograph, (b) map of Al, (c) Zn, (d) Mg, (e) Cu, (f) Cr, (g) Zr, (h) Si, (i) Mn.	301
Fig. 5.20	Spectrum area mapping of precipitates after FSP: (a) bright-field STEM micrograph, (b) spectrum of elements in the selected area of precipitates	302
Fig. 5.21	STEM-EDS elemental mapping of precipitates after FSP: (a) bright-field STEM micrograph, (b) map of Al, (c) Zn, (d) Mg, (e) Cu, (f) Cr, (g) Zr, (h) Si, (i) Mn.	303
Fig. 5.22	Changes of hardness in AR alloy (a), after 1 pass FSP (b),	305-306

	after 2passes of FSP (c), after 3 passes of FSP (d), changes of residual stress along the TD of processed alloy (f), changes of RS from NZ after multi-pass FSP.	
Fig. 5.23	(a) Engineering stress vs. engineering strain plots for AR alloy, and after FSP, log true stress vs. log true plastic strain plot calculated from experimental data and flow curve as per Hollomon, Ludwik, Swift, Ludwigson, and Voce models for (b) AR alloy, and (c) after FSP.	307-310
Fig. 5.24	Hardening rate ($d\sigma/d\varepsilon$) vs. true plastic strain plot (ε_p) of AR alloy (a), $\ln(d\sigma/d\varepsilon)$ vs. $\ln(\varepsilon_0+\varepsilon_p)$ plot, after 1pass FSP (b), 2pass FSP (c), and 3pass FSP(d) showing three stages of hardening behavior, (e) combined $\ln(d\sigma/d\varepsilon)$ vs. $\ln(\varepsilon_0+\varepsilon_p)$ plot after FSP.	311-314
Fig. 5.25	Fractography of AR alloy (a,b), 1 pass FSP (c, d), 2 pass FSP (e,f), 3passes FSP (g, h).	316-317

List of the Tables

	Tables caption	Page No
Table 1.1	Wrought Al-alloys designation system	3
Table 1.2	Temper designations of the heat-treatable Al-alloys	5
Table 1.3	Letters used for illustrating the work hardenable/non-heat treatable Al-alloys	6
Table 1.4	The solid solubility of major alloying elements in α -Al	7
Table 1.5	Structure-property requirements for the modern aircraft design	10
Table 1.6	Applications of conventional age hardenable Al alloys in airframe structures	19
Table 1.7	Comparison of specific properties of heat-treatable Al-alloys	21
Table 1.8	Metastable precipitation sequences in the age-hardenable Al-alloys	23
Table 1.9	Crystallographic information of the precipitates	23
Table 1.10	Crystallographic data of Al-Mn alloy system	25
Table 1.11	Mechanical properties of the aged 7xxx series Al-alloys	35
Table 1.12	Typical FCC re-crystallization and deformation textures	42
Table 1.13	Typical FCC deformation textures in metals and alloys	43
Table 1.14	Important fiber textures in FCC-based metals, and alloys	45
Table 1.15	Atomic radii of alloying elements in 7xxx series Al-alloys	50
Table 2.1	Chemical compositions of the AR alloy AA7075T7352 (Wt%).	65
Table 3.1	d-spacing value of precipitates, and respective JCPDS card number	129
Table 3.2	Size of precipitates in as-received state and D ₂ , D ₃ , and D ₄ specimens	154
Table 3.3	Tensile properties of the fractured specimen D ₁ of AA7075T7352	154
Table 3.4	Precipitates size in T4, T6, T73 and T7352 tempered Al-alloys	173
Table 3.5	Tensile properties of the heat-treated 7075 Al-alloy	179
Table 3.6	Work hardening parameters of the heat-treated 7075 Al alloy	181
Table 3.7	Work hardening parameters of slopes, transition strain, and work hardening rates	185
Table 3.8	Slope (<i>m</i>), and intercept of stage III, hardening rate (θ), and transition true strain (ϵ_r) after every stage of the Ludwigson fitted curve	187
Table 3.9	Stress corrosion severity of AA7075 at T4, T6, T73, and T7352 tempers	190
Table 4.1	Lattice micro-strain, crystallite size, and dislocation density of	226

	heat-treated and thermo-mechanically processed 7075 Al-alloys	
Table 4.2	The volume fraction of precipitates after heat treatments and thermo-mechanical processing	227
Table 4.3	Tensile properties of 7075 Al alloy after heat treatments (T4, T6) and thermo-mechanical processing (TMP-1, TMP-2, and TMP-3)	241
Table 4.4	Flow parameters of the best-fitted mathematical models of heat-treated and TMP	244
Table 4.5	The magnitude of the slopes, transition strain, and hardening Rate of the Swift fitted curve	247
Table 4.6	The slope, intercept, transition strain (ε), and hardening rate (Θ) of the Ludwigson fitted flow curves.	250
Table 5.1	Lattice micro-strain (ε), crystallite size (D in \AA), and dislocation density	270
Table 5.2	Texture components, orientation, and relative intensity of AR alloy	273
Table 5.3	Texture components, orientation, and relative intensity after 1 pass FSP	275
Table 5.4	Texture components, orientation, and relative intensity after 2 pass FSP	277
Table 5.5	Texture components, orientation, and relative intensity after 3 pass FSP	279
Table 5.6	Tensile properties of AR alloy, and after multi-pass FSP	310
Table 5.7	Best fitted flow curve parameters in AR state, and after multi-Pass FSP	314
Table 5.8	Intercept and slope of the linear portion of stages II and III, as well as Θ and ε_r at the end of all stages.	316

List of Symbols

$^{\circ}\text{C}$ Degree centigrade

μm Micrometer

nm Nanometre

α Alpha

θ Theta

Wt% Weight percent

kHz Kilo Hertz

mHz Mili Hertz

mg Milli gram

mm Milli meter

ml Mili liter

t Time (h)

A Area (cm^2)

a, b, c Lattice parameters

D (\AA) Average crystallite size (in angstrom)

D_{av} Average grain size

cm Centimetre

hrs Hours

S Second

\geq Greater than

\leq Less than

b Burger vector

λ Wavelength

ϵ Lattice micro-strain

β Beta

η Eta

η' Eta prime

MPa Mega Pascal

H_v Hardness in Vickers scale

T_r Transition strain

v Poison's ratio

E Youngs Modulus

G Shear Modulus

HAGBF = High-angle grain boundary fractions

LAGBF = Low-angle grain boundary fractions

Abbreviations

ASTM	American Society for Testing and Materials
EBS	Electron Back Scattered Diffraction
EDS	Energy Dispersive Spectroscopy
FCC	Face Centred Cubic
FESEM	Field Emission Scanning Electron Microscope
GP zone	Guinier Preston Zone
HAADF	High Angle Annular Dark Field
HCP	Hexagonal Close Packing
HRTEM	High-Resolution Transmission Electron Microscope
FFT	Fast Fourier Transform
FSP	Friction Stir Processing
RPM	Rotation Per Minutes
SAEDPs	Selected Area Electron Diffraction Patterns
SCC	Stress Corrosion Cracking
TEM	Transmission Electron Microscope
STEM	Scanning Transmission Electron Microscope
XRD	X-ray Diffractometer
WB	Weak Beam
WBDF	Weak Beam Dark Field
HR- XRD	High-Resolution X-Ray Diffractometer

OIM	Orientation Imaging Microscopy
FSP	Friction Stir Processing
FSPed	Friction Stir Processed
KAM	Kernel Average Mis-orientation
CSL	Co-incidence Site Lattice
EBSD	Electron Back Scattered Diffraction
ODF	Orientation Distribution Function
GND	Geometrically Necessary Dislocation
DRx	Dynamic Re-crystallization
CDRx	Continuous Dynamic Re-crystallization